Porcacchia Leonardo (Orcid ID: 0000-0001-5208-4283)

Investigating the GPM Dual-Frequency Precipitation Radar Signatures of Low-Level Precipitation Enhancement

Leonardo Porcacchia[1], P.E. Kirstetter[2,3], V. Maggioni[1], S. Tanelli[4]

[1]Civil, Infrastructure and Environmental Engineering Department, George Mason University, Fairfax, VA

[2]Advanced Radar Research Center, National Weather Center, Norman, OK

[3]NOAA/National Severe Storms Laboratory, Norman, OK

[4]Jet Propulsion Laboratory, California Institute of Technology, Pasadena, CA

Corresponding author:

Leonardo Porcacchia, George Mason University

4400 University Drive, Fairfax, VA 22030, Nguyen Engineering Building, Room 4603

Email: lporcacc@gmu.edu

Running Head: GPM DPR Signatures of Low-Level Precipitation Enhancement

This is the author manuscript accepted for publication and has undergone full peer review but has not been through the copyediting, typesetting, pagination and proofreading process, which may lead to differences between this version and the Version of Record. Please cite this article as doi: 10.1002/qj.3611

Key Words: Precipitation enhancement; collision-coalescence; radar; GPM; DPR; microphysics

Abstract

High-intensity precipitation represents a threat for several regions of the world because of the related risk of natural disasters (e.g., floods and landslides). This work focuses on low-level precipitation enhancement that occurs in the cloud warm layer and has been observed in relation to collision-coalescence (CC) leading to flash floods and extreme rainfall events in tropical and temperate latitudes. Specifically, signatures of precipitation enhancement (referred to as CC-dominant precipitation) are investigated in the observations from the Global Precipitation Measurement (GPM) core mission Dual-frequency Precipitation Radar (DPR) over the central/eastern Contiguous United States (CONUS) during June 2014 – May 2018. A classification scheme for CC-dominant precipitation, developed for dual-polarization S-band radar measurements and applied in a previous work to X-band radar observations in complex terrain, is used as a benchmark. The scheme is here applied to the GPM ground validation dataset that matches ground-based radar observations across CONUS to space-borne DPR retrievals. The occurrence of CC-dominant precipitation is documented and the corresponding signatures of CC-dominant precipitation at Ku- and Ka-band are studied. CC-dominant profiles show distinguishing features when compared to profiles not dominated by CC, e.g., characteristic vertical slopes of reflectivity at Ku- and Ka-band in the liquid layer, lower freezing level height, and shallower ice layer, which are linked to environmental conditions driving the peculiar CC microphysics. This work aims at improving satellite quantitative precipitation estimation, particularly GPM retrievals, by targeting CC development in precipitation columns.

1. Introduction

Precipitation is a key component of the global water cycle and understanding its nature and the atmospheric processes behind its development is a critical challenge of our times. High-intensity precipitation, in combination with flooding-prone geographical areas and increasing population demographics, may lead to human and economic losses (Gochis et al., 2014; Gourley et al., 2016; Saharia et al., 2017; Terti et al., 2017; Warner et al., 2000). The risk of natural hazards is augmented by the radicalization of severe weather events in the last decades due to climate change (IPCC, 2014). The necessity of accurate quantitative precipitation estimation (QPE) and improved observations of precipitation processes at the global scale is thus undeniable (National Academies of Sciences, 2018), especially in those regions where ground measurements and hazard protection resources are scarce. Accurate QPE is essential for hydrological applications, climate studies, water resources management, and weather forecasts on which we rely daily (Hong et al., 2007; Hou et al., 2008; Lebel et al., 2009; Stephens & Kummerow, 2007).

Remote sensing instruments have been used for decades to monitor precipitation all over the globe. They provide indirect measurements of precipitation across widespread regions with good spatiotemporal resolution. Particularly, meteorological radars are active remote sensors that rely on the scattering of the deployed electromagnetic beam on atmospheric particles. Common issues with ground-based radars, such as partial beam blockage due to orography and complex terrain deployment (Zhang et al., 2014), can be overcome using space-borne radars. Nevertheless, retrievals from the latter often show spatial and temporal resolutions lower than the

typical scale of the targeted precipitation variability (Derin & Yilmaz, 2014; Kirstetter et al., 2015b; Maggioni, Sapiano, & Adler, 2016). Furthermore, transforming remote-sensing observations into actual rainfall rate products is based on a priori assumptions on the typology of precipitation (ongoing microphysical processes) and introduces unavoidable uncertainties (Anagnostou et al., 2013; Kirstetter et al., 2015a; Le & Chandrasekar, 2013; Zhang, Qi, Kingsmill, & Howard, 2012; Zhang et al., 2014).

Precipitation is usually classified into two broad categories, namely stratiform and convective. Stratiform precipitation is characterized by long lasting, low intensity showers occurring in a stable environment. In a cloud with temperatures lower that 0°C, where the water droplets are supercooled and ice and liquid phase particles coexist, the Bergeron process (or "cold-rain process"; Houghton, 1951) plays a fundamental role in efficiently increasing the crystals size due to accretion. Such crystals eventually start precipitating and may or may not melt in the cloud melting layer (ML) before reaching the surface as rain or snow. Convective precipitation, on the contrary, develops in unstable and moist atmospheres where strong updrafts mix hydrometeors and lift large particles upward. It usually falls as showers limited in spatial extension and duration. It is associated with thunderstorms, high-intensity rainfalls, and sometimes hail or graupel.

A third precipitation category has recently drawn the attention of operational weather services and researchers because of its widespread and threatening features. Hamada et al. (2015) showed that the highest rainfall rates in the tropics and subtropics are attributable to low-echo

centroid (LEC) systems, rather than to purely convective precipitation. Environmental conditions associated with LEC systems are high lower-atmosphere moisture concentrations, high relative stability, and large liquid layer extension (Gochis et al., 2014; Grams et al., 2014; Petersen et al., 1999; Vitale & Ryan, 2013). The same signatures have been observed in warm-rain (tropical) precipitation systems, which indicate intense rainfall events originated by clouds with temperatures everywhere higher than 0°C. Despite this definition, such systems have often been observed to extend above the 0°C isotherm level and include ice phase hydrometeors (Carr et al., 2017; Porcacchia et al., 2017).

The three precipitation regimes sometimes occur within the same system (e.g., in a Mesoscale Convective System) and the definitions given above may overlap, resulting in misclassification and precipitation retrieval inaccuracy. From a microphysical point of view, many processes are involved, but our knowledge of them is limited by the available information from the observing sensors. For instance, with radar observations, convective precipitation is recognizable by isolated cells of high reflectivity (Z), while stratiform precipitation is characterized by Z peaking in the ML, indicative of a well-defined bright band (BB) region, and lower elsewhere. Nevertheless, convective and tropical precipitation can show a radar BB signature as well and Z values below the BB similar to stratiform precipitation (Xu et al., 2008). Additional microphysical information is thus necessary to distinguish the precipitation typology.

A characterization of precipitation regimes based on the signatures of the microphysical processes involved is proposed here to improve classification and rain rate retrievals.

Particularly, we focus on warm-rain processes that take place in the liquid layer of a cloud (e.g., collision-coalescence, evaporation, breakup, and size sorting). Collision-coalescence (CC) is responsible for efficient drop-size increasing towards the ground and is the main cause of low-level precipitation enhancement (Stoelinga et al., 2013). In a precipitation column dominated by CC, the drops that have grown enough due to chaotic collisions start to precipitate towards the surface and collect smaller particles in their descent, resulting in rainfall rate enhancement. CC tends to be dominant in marine clouds, but also overland at mid- and intertropical-latitudes in clouds extending above the 0°C isotherm level (Carr et al., 2017), and in mountainous regions where warm moist air is lifted due to orography (Erlingis et al., 2017; Porcacchia et al., 2017).

Several studies have attempted to identify warm-rain/tropical precipitation leading to low-level enhancement. A first type of classification scheme relied on active/passive observations from satellite-based sensors and on the assumption that warm-rain precipitation is characterized by the absence of an ice phase (Liu & Zipser, 2009). Unfortunately, such type of scheme was effective only for tropical/oceanic clouds. Xu et al. (2008) extended their search for warm-rain precipitation to CONUS by analyzing vertical profiles of reflectivity (VPR) from the Next Generation Weather Radar (NEXRAD) network. Z was shown to increase toward the surface in the liquid layer most probably due to CC. Their efforts were complemented by Grams et al. (2014) who introduced environmental variables to segregate conditions in which warm-rain processes are likely to develop and defined the probability of warm-rain (POWR). The NOAA National Severe Storm Laboratory (NSSL) Multi-Radar Multi-Sensor (MRMS) system, which

integrates about 180 operational radars across CONUS (and southern Canada), currently employs POWR to identify seven different types of surface precipitation, including tropical stratiform and tropical convective (Zhang et al., 2015). Nevertheless, the main limitations of the abovementioned works are the use of single-polarization radar observations (despite the polarimetric capability of the operational radars) and the restricted applicability to central/eastern CONUS. Carr et al. (2017) and Porcacchia et al. (2017) proposed a classification scheme for warm processes based on polarimetric retrievals from the NEXRAD network over eastern CONUS and from the NOAA/NSSL X-band polarimetric radar (NOXP) deployed in the 2014 IPHEx North Carolina field campaign, respectively. They showed that it is possible to detect low-level precipitation enhancement by analyzing the vertical evolution of the reflectivity factor at horizontal polarization (Z_h) and of the differential reflectivity (Z_{dr}) in the cloud liquid layer. However, they did not guarantee that the observed precipitation enhancement was due to CC development alone. That is why it is advisable to refer to these precipitation systems as CC-dominant.

This work is intended to extend the detection of low-level enhancement signatures to space-borne sensors. We focus on the Global Precipitation Mission (GPM; Hou et al., 2013) core observatory, a National Aeronautic and Spatial Administration (NASA) – Japanese Aerospace Exploration Agency (JAXA) joint mission launched in orbit around the Earth on February 27th 2014, which hosts the first space-borne Dual-frequency Precipitation Radar (DPR). Kobayashi et al. (2018) analyzed DPR Ku-band VPRs below the BB and observed a significant fraction of

profiles with reflectivity increasing toward the ground over the North American continent. Such behavior was explained with raindrop size increase due to CC triggered by large-scale upwards motion in the lower troposphere. This study looks at the DPR reflectivity profiles at both Ku- and Ka-band for the sake of completeness. Low-level precipitation enhancement signatures are first identified with dual-polarization radars at the ground and the corresponding signatures in the DPR observations from space are then documented. The goal is to identify CC-dominant precipitation in the DPR dataset and isolate its characteristics. More generally, this effort is aimed at improving remote-sensing based QPE by identifying specific precipitation processes (e.g., CC) that are not parameterized in satellite retrieval algorithms but represent the dominant component of warm-rain/tropical precipitation. The next section (2) introduces the dataset matching ground-based polarimetric radar measurements and space-borne DPR observations. The methodology is described in section 3. Results are shown and discussed in section 4, and conclusions are drawn in section 5, which also discusses future challenges.

2. Data

The proposed approach identifies low-level precipitation enhancement (CC-dominant precipitation hereinafter) by using ground-based radar polarimetric observations and the classification scheme adopted by Porcacchia et al. (2017) and Carr et al. (2017), and then matches the corresponding precipitation profiles with the space-borne radar observations from GPM DPR. The ground-based selection of profiles allows isolating CC-dominant precipitation

and studying its signature in the DPR retrievals.

The NOAA Weather Surveillance Radar-1988 Doppler (WSR-88D) network, known as NEXRAD, provides ground-based polarimetric radar observations. NEXRAD includes 160 S-band Doppler radars distributed across the US and updated to polarimetric capability by the end of 2013. The WSR-88D radars operate at 2.7-3.0 GHz and scan the atmosphere at antenna elevations varying from 0.5º to 19.5º. We will refer to WSR-88D as ground radar (GR) hereinafter.

GPM DPR consists of the Ku-band precipitation radar (KuPR, operating at 13.6 GHz) and the Ka-band precipitation radar (KaPR, operating at 35.5 GHz). A KuPR scan comprises 49 beams in the azimuthal angle interval of ±17º cross track and each beam identifies a separate footprint of approximately 5 km diameter at the earth surface. The KaPR provides measurements in two scan modes: matched scan (MS) and high-sensitivity scan (HS). In the MS mode, KaPR identifies 25 footprints co-aligned with the inner KuPR footprints. Both KuPR and KaPR scan the atmosphere at vertical range steps of 250 m and zenithal angles varying between ±8.5º cross track. The HS mode is used for detecting light rain and snow and the KaPR beams are interlaced within the scan pattern of the MS beams. The vertical range resolution is 500 m.

2.1 Matched Dataset

The matched dataset provided by the GPM ground validation network (VN) is used in this study

(ftp://hector.gsfc.nasa.gov/gpm-validation/). The VN performs a direct spatiotemporal matchup of DPR and GR measurements (as described in detail at https://pmm.nasa.gov/sites/default/files/document_files/Val_Network_Users_Guide_Vol_2_Nov 2015.pdf). For sake of simplicity, we will name this matched-up dataset DPR-GR hereafter. The matching procedure is applied to a total of 75 GRs distributed over the US and other regions from international networks. This work focuses on central/eastern CONUS (no access was guaranteed to GR observations in the central/western part) and all the match-ups between DPR and GR from June 2014 to May 2018 are used. Figure 1a displays the overpass of DPR over GR locations for a specific orbit on 06/02/2015. The DPR-GR dataset archives GR uncorrected polarimetric variables and DPR level 2 retrievals (Iguchi et al., 2016). Version 6 DPR data in the MS scan mode were selected in this work.

The geometry matching technique to match observations at the same location, time, and resolutions from ground and space is described in Bolen & Chandrasekar (2003) for the Tropical Rainfall Measurement Mission (TRMM) Precipitation Radar (PR), and was adapted to GPM-DPR by Morris & Schwaller (2011) to derive the DPR-GR dataset. Firstly, all the DPR range bins for a fixed beam/footprint intersected by one GR sweep at a given antenna elevation are averaged along the vertical over the GR width (Fig. 1b). The DPR-GR matched volume comprises a “waffle” of GR measurements over the DPR footprint (Fig. 1c). Secondly, ground polarimetric measurements exceeding a fixed threshold (specific to each variable) are averaged over the waffle in a single value to compare with the DPR measurements. Additional information

is derived for each radar polarimetric variable, including the total number of bins within a waffle, the number of bins exceeding the threshold (non-missing bins), and the standard deviation along with the averaged value. Only the 25 DPR inner profiles belonging to the MS scan mode are used to match GR observations with DPR retrievals at Ku- and Ka-band. Iguchi et al. (2016) describe the processing of DPR retrievals in a series of hierarchical modules that compose the DPR level 2 retrieval algorithm.

In general, six DPR variables would be of interest for this type of study. Two are the direct observables, that is, the measured effective (or equivalent) radar reflectivity factor at Ku- and Ka-band (as defined for example in Meneghini & Kozu, 1990). In one of the preparatory modules of the DPR algorithm (i.e., the Vertical Profile Module) these are corrected only for the attenuation introduced by water vapor, molecular oxygen, and cloud liquid water estimated from general circulation model inputs. These corrections are in general small (i.e., less than 2 dB at Ka-band, and much less than 1 dB at Ku band). The resulting variables will be referred to hereinafter as the 'measured reflectivities', Z_m, in dBZ. Their Dual Frequency Ratio – i.e., the base 10 logarithm difference between Z_m(Ku) and Z_m(Ka) – will be indicated by DFRm.

The next three variables are derived from them: the attenuation corrected effective (or equivalent) radar reflectivity factor (hereinafter 'corrected reflectivity', Z_e, in dBZ) at Ku- and Ka-band, and their difference (DFR_e, in dB). These are all are produced by the DPR algorithm after a complex set of modules that aim at classifying and estimating microphysical properties. While ideally the analysis of Z_e and DFR_e would lend itself more readily to interpretation in

terms of mean particle sizes and particle number concentrations, its use in this case is challenged by the fact that we apply a complex retrieval algorithm about microphysics which do not consider collision-coalescence processes. Notably, the Classification Module within the DPR level 2 algorithm does not include a parameterization for CC-dominant precipitation or, more generally, warm-rain. Precipitation is classified as two main categories (stratiform and convective), plus the "other" category that accounts for precipitation detected only at altitudes higher than the 0˚C level or noisy data (Awaka et al., 2016). As discussed in the previous section, CC processes can occur in pure warm-rain conditions, or in the liquid-layer of cold-rain columns. Furthermore, the level 2 algorithm Solver Module operates with regularization constraints that limit the degrees of freedom by which the retrieved microphysical properties can vary along a profile. Therefore, these become confounding factors and may create a circular problem when our intent is first and foremost to identify whether CC processes do leave a detectable signature on the DPR data.

On the other hand, the use of 'measured' reflectivities offers a more direct means to identify observable characteristics modes associated to CC, if any. However, the resulting salient features must be carefully interpreted in light of the attenuation that affects them. Their use will be explicitly specified throughout the manuscript.

2.2 Quality Controls

The GR polarimetric variables to detect CC-dominant precipitation are Z_h and Z_{dr}. Z_h (dBZ)

depends on the concentration, size, state, and shape of particles in the radar volume. Z_{dr} (dB) is defined as the difference between the reflectivity factors at horizontal and vertical polarization. It provides insight of the raindrop average size in the radar volume, as well as the spatial orientation of maximum dimension. Before using the GR data as input to the scheme for CC-dominant precipitation, several quality control steps are germane:

- Only data within 60 km from each GR location are selected, in order to ensure scanning the lower levels of the atmosphere (liquid layer) and to limit the effects of radar beam broadening (Kirstetter et al., 2013);
- The volume filling is defined as the percentage of bins in the waffle with Z_h values greater than 15 dBZ and non-missing values for the other polarimetric variables as Z_{dr}. Only data from volumes filled more than 75% are selected to ensure representativeness of the measurements in each waffle;
- The standard deviation of the radar variables computed within each waffle is also used to ensure the representativeness of the values. Only data with standard deviation less than the first quartile of such distribution are selected, in order to limit the horizontal variability within the waffle.
- Hydrometeor type information available for each bin within a waffle is used to restrict the analysis to liquid precipitation. For a given profile, only waffles with at least 80% of the bins belonging to liquid hydrometeor categories (either rain or drizzle) are selected.

3. Methodology

The polarimetric classification scheme for CC-dominant precipitation introduced by Carr et al. (2017) and adapted to complex terrain by Porcacchia et al. (2017) relies on the microphysical interpretation of the vertical variations of Z_h and Z_{dr} in the liquid layer. Every microphysical process that develops in the liquid layer (e.g., collision-coalescence, evaporation, breakup, and size sorting) shows a peculiar signature in terms of the abovementioned variables. Particularly, CC is related to an increase of both Z_h and Z_{dr} towards the surface (Kumjian et al., 2012) corresponding to negative slopes in the vertical profiles of Z_h and Z_{dr} when the atmospheric height is measured from the ground upwards. In the (ΔZ_h, ΔZ_{dr}) parameter space (Kumjian & Prat, 2014) the CC process is represented by the first quadrant, where the variation of both polarimetric variables Z_h and Z_{dr} towards the surface is positive (Figure 2). For each profile, ΔZ_h and ΔZ_{dr} are calculated between the height just below the ML bottom and the clutter free height closest to the ground. 53.7% of the precipitation profiles selected for this study are dominated by CC. The selection procedure for these profiles is described below.

Vertical profiles of Z_h and Z_{dr} are calculated for each precipitation column, together with their slopes in the liquid layer. Because slanted precipitation can impact the slopes of Z_h and Z_{dr} and induce false detection of CC, slopes are also extracted from the four neighboring columns (two along and two cross track direction of GPM) and compared to the one under investigation. When the slopes of Z_h and Z_{dr} are both negative within the studied column and in the

neighboring columns, a CC-dominant profile is identified. Likewise, a non-CC-dominant (NCC) profile is identified when at least one between the slopes of Z_h and Z_{dr} is positive within the studied as well as the neighboring columns. Precipitation columns where the slopes of Z_h and Z_{dr} profiles are inconsistent among neighboring columns are set aside. The set of NCC profiles, complementary to the set of CC-dominant profiles, represent precipitation columns where microphysical processes other than CC are dominant. A total of 797 profiles are identified as CC-dominant and 644 as NCC. The limited sample is due to the conservative quality controls described in section 2.2. In addition, at least two measurements in the liquid layer are required to calculate the slopes of Z_h and Z_{dr} profiles, which reduces significantly the sample size. As a result, caution is needed in interpreting the proportion of NCC profiles to CC-dominant profiles.

Note that this is a tentative classification and does not guarantee the identification of CC alone, whose signatures might overlap with breakup's (Kumjian & Prat, 2014). The (ΔZ_h, ΔZ_{dr}) parameter space methodology targets drop-size increase and thus precipitation enhancement, which are better described as CC-dominant precipitation.

Once CC-dominant and NCC profiles are identified thanks to GR polarimetric measurement, the corresponding DPR columns are extracted from the DPR-GR dataset and analyzed to study the space-borne signatures of CC-dominant precipitation.

Figures 3a-b show an example of vertical profiles of Z_h and Z_{dr} for a precipitation event observed on 03/09/2014 in Wisconsin, USA (latitude 45.32 N, longitude 98.36 W). The liquid layer goes from the BB bottom to the highest height between the ground clutter-free level and 1

km. The increase in both Z_h and Z_{dr} in the liquid layer, consistent with the neighboring columns (not shown), identifies this precipitation column as CC-dominant. The analysis of the profile of $D_{m,GR}$, the mean diameter obtained from GR polarimetric observations, confirms that drops are increasing in size in the liquid layer towards the surface due to CC (Fig. 3c). DPR retrievals of the same event are displayed in Figures 3d-f. In Figure 3f, $D_{m,DPR}$ refers to the median diameter retrieved by the Solver Module within the DPR level 2 algorithm. While the attenuation corrected reflectivity Z_e increases in the liquid layer towards the ground at both Ku- and Ka-band, the trend of the measured reflectivity Z_m is not straightforwardly increasing. At Ka-band the attenuation effect is particularly noticeable and results in decreasing reflectivity. The lack of an obvious marker of CC is part of the reason why this specific process, which is the basis for the low-level precipitation enhancement, is challenging for the GPM products. The current DPR level 2 retrieval scheme does not account for the nature of CC microphysics and models the DSD of the selected event with a stratiform parameterization (this specific profile is classified as stratiform from the Classification Model). It contributes to the difference of about 0.3 mm in the overall values of $D_{m,GR}$ and $D_{m,DPR}$. Nevertheless, the Solver Module is able to capture the trend in the drop median volume that shows a slight increase towards the surface (a direct consequence of the DFR_e profile in the liquid layer), consistent with GR polarimetric observations.

Figure 4 presents cross-track and along-track DPR observations for the 03/09/2014 precipitation event. Figures 4a and 4b show Z_m(Ka) and Z_m(Ku), respectively, as a function of the GPM cross-track scanning coordinate (x-axis) and the atmospheric height (y-axis). Similarly,

Fig. 4c and 4d show the reflectivity profiles along track. Reflectivity is clearly less attenuated at Ku-band and allows to distinguish a BB extending in both cross- and along-track directions for at least 45 km at a height of about 4.5 km. Below the BB, reflectivity reaches 50 dBZ that is close to the BB peak value. Some of the precipitation columns neighboring the studied column (indicated by a black vertical line) manifest the same increasing trend in reflectivity highlighted in Fig. 3d. The precipitation column (profile) is part of a larger system extending for at least 150 km in both directions and characterized by convective cores as well as stratiform-like BB regions in which signatures of CC development are detected.

4. Results

Figure 5 shows the spatial distribution of CC-dominant and NCC profiles during spring (MAM), summer (JJA), fall (SON), and winter (DJF). Profiles are accumulated within grid boxes of 5º latitude × 5º longitude; the size of the markers is proportional to the number of events and the symbol refers to the precipitation category with the highest occurrence (circles for CC-doninant and triangles for NCC). CC-dominant events are scattered across the central/eastern CONUS with different distributions during the four seasons; they are quite frequent and ubiquitous in spatial occurrence. Nevertheless, at central longitudes and central/northern latitudes (corresponding approximately to the states of Kansas, Nebraska, Iowa, Minnesota, and Wisconsin), CC-dominant profiles outnumber NCC profiles throughout the entire year. It is also remarkable that the amount of detected profiles is higher during the cold seasons (fall and winter,

Fig. 5c and 5d, respectively). This is probably a consequence of the adopted quality control that excludes data with low horizontal homogeneity, penalizing warm-season baroclinic frontal instabilities and turbulent mixing. Furthermore, during winter, CC-dominant events tend to concentrate in the southeastern CONUS. This can be imputed to the proximity to the ocean, which provides a supply of moisture in the lower atmospheric levels to trigger CC development, and to the higher ML depth (Grams et al., 2014). On the other hand, during the warm seasons (spring and summer, Fig. 5a and 5b, respectively) there is no dominance of CC-dominant events in the same coastal regions. Further analysis is required to properly investigate this point.

4.1 Vertical Profiles of Reflectivity

In the following is presented a comparison of vertical profiles of Z_m and DFR_m between CC-dominant and NCC profiles. NCC profiles include mostly stratiform precipitation according to the Classification Module within the DPR level 2 algorithm (only 1 profile is classified as convective). Furthermore, the majority of CC-dominant profiles are classified as stratiform from the same DPR algorithm. The intention here is to investigate the separation between CC-dominant and NCC profiles in terms of observations in the DPR profiles.

VPRs are extracted for CC-dominant and NCC profiles from Z_m(Ku) and Z_m(Ka) observations at varying heights. The conditional distributions for the vertical profiles of measured reflectivity and DFR_m are shown in Fig. 6. DFR_m (dB) is largely used by the GPM community to separate liquid and solid precipitation. Particularly, DFR_m plays a fundamental

role in the DPR level 2 retrieval algorithm for attenuation correction and BB identification (Awaka et al., 2016). Figures 6a and 6b show VPRs at Ku- and Ka-band, respectively. The median, 25th and 75th quantiles of reflectivity, as well as the 0ºC level, are presented. The y-axis represents the height relative to the 0ºC level, to mark the difference between the reflectivity behavior in the cold cloud layer and in the melting/liquid layers.

Focusing first on the cold layer, CC and NCC distributions are shifted by about 3 dB. The 25th NCC Z_m quantile aligns well with the 50th CC Z_m quantile. Such difference is slightly reduced at Ka-band, but it is still indicative of either a lower concentration of ice particles in a CC-dominant profile or presence of particles with lower scattering properties. This is consistent with the findings of Carr et al. (2017) that used ground-based S-band radar data for their analysis. In reminding that we are analyzing Z_m (as opposed to Z_e), a specific feature supports this interpretation: the difference in Z_m and DFR_m between CC-dominant and NCC is almost constant in the cold layer, indicating that difference in attenuation effects is negligible (i.e., albeit theoretically possible, it is hard to envision a systematic vertical change in the microphysics that exactly compensates for cumulative attenuation effects in an almost identical fashion in the two cases).

Regarding the ML, NCC profiles manifest a clear BB just below the 0ºC isotherm at Ku-band, while for CC-dominant profiles the BB is less pronounced and narrower. This is consistent with the melting of a reduced ice content or possibly with the melting of smaller frozen hydrometeors.

The most evident signatures separating CC-dominant from NCC profiles appear in the liquid layer. Consistent with S-band reflectivity profiles (Xu et al., 2008), Ku-band Z_m increases in the liquid layer towards the surface for CC-dominant profiles, while a decreasing trend is observed for NCC profiles. A similar but less evident difference is noticeable at Ka-band, i.e., the CC-dominant profiles have a "less positive" slope in the liquid layer than the NCC. Interestingly, the DFR_m vertical profiles do not show significant differences between non-CC dominant and NCC (Fig. 6c). Since these are profiles affected by precipitation-induced attenuation, they must be interpreted accounting for it. First, we note that in general these cases cluster below 35 dBZ at the top of the liquid layer: in these regimes, specific attenuation at Ku-band is less than 0.15 dB/km (see e.g., Meneghini & Kozu, 1990), and therefore a negligible contributor compared to the observed features. At Ka-band, rain-induced attenuation can be 6-10 times larger than at Ku-band, it therefore spans a significant range from less than 0.2 dB/km for Z_e(Ku) around 25 dBZ to almost 1 dB/km at around 35 dBZ. These numbers provide general bounds to interpret the liquid layer in Figure 6: Z_m(Ku) increases towards the surface in CC-dominant profiles by 4-6 dB more than NCC, a difference that cannot be attributed to attenuation; a similar statement is valid at Ka, but those slopes are clearly modulated also by the attenuation towards lower numbers. These features point at breakup and evaporation processes dominating the evolution of NCC cases, while CC processes dominate the CC-dominant profiles. It is interesting to note that the behavior of DFR_m is almost identical between CC-dominant and NCC, indicating that, for this specific process, the attenuation and differential scattering compete

against each other and resulting in the DFR_m being an inconclusive observable. If we name A(Ku) and A(Ka) the path attenuation from the radar to the range of interest r at Ku- and Ka-band, respectively, then DFR_m=DFR+delA, where delA=A(Ka)-A(Ku). The delA term often dominates the behavior of DFR_m and is not directly related to the DSD characteristics at the range r because it depends on the hydrometeors along the path from the radar to the range r. While DFR is closely related to Dm at the range of interest, DelA plays a fundamental role in masking the DFR behavior, which is supposed to increase with increasing D_m due to CC.

A closer look at the CC-dominant and NCC data sets is required to account for the individual characteristics of the precipitation columns. As shown in Fig. 5, the precipitation cases selected for this study belong to different seasons and locations and therefore need to be assessed separately. The vertical slopes of reflectivity at Ka- and Ku-band, as well as the slopes of DFR_m, are calculated in the cold and warm layers for each precipitation column and their distributions are presented in Fig. 7. The ice layer is defined as the vertical portion of the atmosphere between the storm top height (STH) and a 0.5-km reference height above the 0ºC level (Fabry & Zawadzki, 1995). The liquid layer extent, as abovementioned, is limited by the ground clutter. Among all the distributions shown in Fig. 7, the CC and NCC distributions of reflectivity slope at Ku- and Ka-band in the liquid layer (Fig. 7a and 7b, respectively) appear to be more clearly separated.

The two-sample Kolmogorov-Smirnov (2KS) test was applied to each pair of distributions to assess the degree of separation between them, and the asymptotic significance

parameter (p-value) was calculated. The p-values, as well as the median and standard deviation (SD) of the distributions, are presented in Table 1. As expected, the slopes of reflectivity at Ku- and Ka-band in the liquid layer show very small p-values (<1.0e-15) indicating a low probability for CC-dominant and NCC distributions of belonging to the same parental distribution. On the contrary, p-values are higher for DFR_m slopes in both liquid and ice layers and median values of CC-dominant and stratiform slopes are similar. This means that the DFR_m slopes, and more generally the DFR_m profiles, are a worse discriminant between CC-dominant and NCC precipitation than Ku- and Ka-band profiles of reflectivity. This result is not intuitive in a context where DFR_m is used for classification purposes in the level 2 algorithm.

4.2 Macrophysical Properties

In the previous section, the slopes of reflectivity have been calculated in the ice and liquid layers for CC-dominant and NCC profiles. We now focus on macrophysical characteristics of these layers. The intent is to document the cloud properties (as seen by DPR) of CC-dominant precipitation and compare them to NCC profiles. Among the macrophysical observables studied here, the ML is defined as the BB region of a stratiform precipitation column and its depth usually does not exceed 0.8 km (Wolfensberger et al., 2016), even though the vertical resolution of DPR observations may result in its apparent thickening.

Figure 8 shows CC and NCC distributions of STH (Fig. 8a), as well as ice, melting and liquid layer depths (Figs. 8b-d). The median and SD of each distribution are presented in Table

2, together with the 2KS p-values for each CC/NCC pair of distributions. First off, the distributions for NCC precipitation have generally a wider spread than the CC-dominant distributions. Recall that these profiles are classified by DPR as stratiform and they may include a variety of precipitation processes and environmental features. According to the parameters with the lowest 2KS p-values (2.56e-15 and 8.22e-15 for STH and ice layer depth, respectively), CC-dominant profiles are characterized by a lower vertical cloud extension and a narrower ice layer. These factors indicate a lower concentration of ice hydrometeors in the column for CC-dominant profiles and are supported by the ML depth distribution that has a lower median value. This is again consistent with the findings of Carr et al. (2017) with ground-based S-band radars. On the contrary, the liquid layer depth is a lesser discriminant to distinguish CC-dominant from NCC profiles.

The reflectivity enhancement in the ML is defined as the difference between the peak of reflectivity (Z_{peak}) and the snow reflectivity (Z_{snow}) just above the BB (Zawadzki et al., 2005). In the case of stratiform precipitation, a decrease in enhancement is related to an increase of the density of ice above the ML (density effect). In this work, the $Z_{m,peak}$ - $Z_{m,snow}$ enhancement has been calculated for CC-dominant and NCC profiles, and its distributions at Ku- and Ka-band are shown in Fig. 8e and 8f, respectively. Median, SD, and 2KS p-values for the CC/NCC pairs are listed in Table 2. The separation in terms of enhancement between CC-dominant and NCC precipitation is weaker if compared to the factors discussed above. Nonetheless, NCC precipitation shows higher median values at both Ku- and Ka-band. In the light of the density

effect, NCC profiles are characterized by a lower ice density than CC-dominant ones above the ML. The presence of larger ice phase particles (more aggregation and less riming) in NCC profiles might explain the lower density and greater extension of the cold layer, as pointed out by VPR and STH. On the contrary, smaller ice phase particles in a CC-dominant profile will result in higher density above the ML and lower extension of the cold layer. Furthermore, a limiting factor to consider in the density effect interpretation is the vertical resolution of DPR.

5. Conclusions

This work investigates precipitation columns characterized by low-level enhancement ascribable to dominance of the collision-coalescence process in the liquid layer and investigates their space-borne radar signatures. The study is performed during June 2014 – May 2018 in central/eastern CONUS. A dataset composed of WSR-88D polarimetric ground radar data matched up with GPM DPR observations is used. Firstly, the polarimetric radar classification scheme developed by Porcacchia et al. (2017) is used to identify CC-dominant events with GR observations. Secondly, thanks to the matched dataset, CC-dominant cases are retrieved within DPR measurements and their signatures at Ku- and Ka-band are studied.

CC-dominant cases occur throughout the entire year within the study region, with a preferable geographical distribution along coastal southern regions during winter, and they often show clear signatures of a BB and an ice phase above it. The measured DPR reflectivity profiles at Ku- and Ka-band are used to juxtapose CC-dominant to NCC profiles. The latter profiles show

higher reflectivity values in the ice layer and a more pronounced ML than CC-dominant profiles. Moreover, the calculated reflectivity slopes in the liquid layer show a significant separation between the two classes of events, with Ku-band reflectivity increasing toward the ground when CC dominates in the liquid layer.

Among the other macrophysical cloud characteristics investigated in this study, the STH and the depth of the ice layer show the highest power to discriminate CC-dominant from NCC profiles. These indicators, together with the reflectivity values observed in the ice and melting layers, point towards a higher ice content for NCC profiles (classically defined stratiform precipitation). This result is expected, since CC is a warm process that does not require cold microphysics to occur in a cloud liquid layer. Nevertheless, CC dominance in the liquid layer does not imply absence of cold processes within the cloud. Further investigation is required to isolate the specific cold processes occurring in CC-dominant columns versus the ice development in stratiform precipitation. Another emerging characteristic of CC-dominant profiles is the increase of reflectivity at Ku-band in liquid layer (at Ka-band the increase is mitigated by a larger attenuation of the radar signal), which corresponds to the increase in Z_h observed at S-band. This work also shows that the DFR_m profiles for CC-dominant and NCC precipitation tend to be very similar in both liquid and ice layers, making this variable less useful for CC-dominant classification.

In the DPR Level 2 retrieval algorithm, the attenuation correction applied to the Ku- and Ka-band VPRs depends on the precipitation typology that is determined by the Classification

Module. In many profiles this attenuation correction is initialized by an estimate of the Path Integrated Attenuation (PIA), which is independent of the microphysical assumptions when derived by one of the Surface Reference Techniques (SRT). If the PIA estimate is accurate, the solutions can be considered independent from the rain-type classification and microphysics. However, in many cases the PIA estimate is affected by sources of error (e.g., partial beam filling and multiple scattering; Battaglia et al., 2015; Battaglia et al., 2016; Kirstetter et al., 2015b) that create significant ambiguities and the deterministic iterative retrieval in the Solver Module has been demonstrated to fail to converge to the correct "epsilon-adjustment" or to converge to obviously erroneous solutions. This is the primary reason why the operational DPR algorithm does have different tables for the different precipitation regimes.

Furthermore, there is one particular aspect that makes proper detection of CC processes even more relevant in this context: even assuming the ideal case where a perfect PIA estimate is provided by the SRT, the DPR algorithm has to apportion part of it to the lowest fraction of the column which is obscured by the surface clutter (because the retrieval starts from the first range bin unaffected by surface clutter). As shown in Figure 6, the occurrence of CC greatly affects the shape of the reflectivity profiles increasingly towards the surface.

An improved classification scheme would account for the occurrence of CC in a precipitation column. Such occurrence in a CC-dominant profile (or a classically defined warm-rain situation), versus CC occurring in a stratiform rain situation, will be possibly associated to different microphysical modes. However, we don't have at this time sufficient statistics to

implement informed specific algorithms and, moreover, such a task is beyond the scope of the present study.

The presented work is limited by the very conservative quality controls applied to the dataset, specifically to GR polarimetric observations. An extension of this study will explore less restrictive conditions on the data (e.g., higher variability in the measurements within the radar volume corresponding to less horizontal homogeneity) and additional profiles that are currently discarded because of slanted precipitation issues. Future work should also focus on the development of a classification algorithm for low-level precipitation enhancement based on the satellite-borne CC-dominant precipitation signatures documented here (e.g., slopes of reflectivity profiles, cloud layer depths, and reflectivity enhancements) to use as input to a machine-learning model.

Acknowledgments

Portion of the research described in this paper was carried out at the Jet Propulsion Laboratory, California Institute of Technology, under contract with the National Aeronautics and Space Administration. The first author would like to thank Dr. Joe Turk, Dr. Sahra Kacimi, and Dr. Ziad S. Haddad for the valuable internship and the help with data quality control. The authors would also like to thank Dr. Robert Morris and Dr. David A. Makofski for the DPR-GR matched dataset (available at ftp://hector.gsfc.nasa.gov/gpm-validation/).

References

Anagnostou, M. N., Kalogiros, J., Marzano, F. S., Anagnostou, E. N., Montopoli, M., & Piccioti, E. (2013). Performance Evaluation of a New Dual-Polarization Microphysical Algorithm Based on Long-Term X-Band Radar and Disdrometer Observations. *Journal of Hydrometeorology*, *14*(2), 560–576. https://doi.org/10.1175/JHM-D-12-057.1

Awaka, J., Le, M., Chandrasekar, V., Yoshida, N., Higashiuwatoko, T., Kubota, T., & Iguchi, T. (2016). Rain Type Classification Algorithm Module for GPM Dual-Frequency Precipitation Radar. *Journal of Atmospheric and Oceanic Technology*, *33*(9), 1887–1898. https://doi.org/10.1175/JTECH-D-16-0016.1

Battaglia, A., Tanelli, S., Mroz, K., & Tridon, F. (2015). Multiple scattering in observations of the GPM dual-frequency precipitation radar: Evidence and impact on retrievals. *Journal of Geophysical Research: Atmospheres*, *120*(9), 2014JD022866. https://doi.org/10.1002/2014JD022866

Battaglia, Alessandro, Mroz, K., Tanelli, S., Tridon, F., & Kirstetter, P.-E. (2016). Multiple-Scattering-Induced "Ghost Echoes" in GPM DPR Observations of a Tornadic Supercell. *Journal of Applied Meteorology and Climatology*, *55*(8), 1653–1666. https://doi.org/10.1175/JAMC-D-15-0136.1

Bolen, S. M., & Chandrasekar, V. (2003). Methodology for Aligning and Comparing Spaceborne Radar and Ground-Based Radar Observations. *Journal of Atmospheric and Oceanic Technology*, *20*(5), 647–659. https://doi.org/10.1175/1520-0426(2003)20<647:MFAACS>2.0.CO;2

Carr, N., Kirstetter, P. E., Gourley, J. J., & Hong, Y. (2017). Polarimetric Signatures of Midlatitude Warm-Rain Precipitation Events. *Journal of Applied Meteorology and Climatology*, *56*(3), 697–711. https://doi.org/10.1175/JAMC-D-16-0164.1

Derin, Y., & Yilmaz, K. K. (2014). Evaluation of Multiple Satellite-Based Precipitation Products over Complex Topography. *Journal of Hydrometeorology*, *15*(4), 1498–1516. https://doi.org/10.1175/JHM-D-13-0191.1

Erlingis, J. M., Gourley, J. J., Kirstetter, P.-E., Anagnostou, E. N., Kalogiros, J., Anagnostou, M. N., & Petersen, W. (2017). Evaluation of Operational and Experimental Precipitation Algorithms and Microphysical Insights during IPHEx. *Journal of Hydrometeorology*, *19*(1), 113–125. https://doi.org/10.1175/JHM-D-17-0080.1

Fabry, F., & Zawadzki, I. (1995). Long-Term Radar Observations of the Melting Layer of Precipitation and Their Interpretation. *Journal of the Atmospheric Sciences*, *52*(7), 838–851. https://doi.org/10.1175/1520-0469(1995)052<0838:LTROOT>2.0.CO;2

Gochis, D., Schumacher, R., Friedrich, K., Doesken, N., Kelsch, M., Sun, J., … Brown, B. (2014). The Great Colorado Flood of September 2013. *Bulletin of the American Meteorological Society*, *96*(9), 1461–1487. https://doi.org/10.1175/BAMS-D-13-00241.1

Gourley, J. J., Flamig, Z. L., Vergara, H., Kirstetter, P.-E., Clark, R. A., Argyle, E., … Howard, K. W. (2016). The FLASH Project: Improving the Tools for Flash Flood Monitoring and Prediction across the United States. *Bulletin of the American Meteorological Society*, *98*(2), 361–372. https://doi.org/10.1175/BAMS-D-15-00247.1

Grams, H. M., Zhang, J., & Elmore, K. L. (2014). Automated Identification of Enhanced Rainfall Rates Using the Near-Storm Environment for Radar Precipitation Estimates. *Journal of Hydrometeorology*, *15*(3), 1238–1254. https://doi.org/10.1175/JHM-D-13-042.1

Hamada, A., Takayabu, Y. N., Liu, C., & Zipser, E. J. (2015). Weak linkage between the heaviest rainfall and tallest storms. *Nature Communications*, *6*, 6213. https://doi.org/10.1038/ncomms7213

Hong, Y., Adler, R. F., Hossain, F., Curtis, S., & Huffman, G. J. (2007). A first approach to global runoff simulation using satellite rainfall estimation. *Water Resources Research*, *43*(8), W08502. https://doi.org/10.1029/2006WR005739

Hou, A. Y., Kakar, R. K., Neeck, S., Azarbarzin, A. A., Kummerow, C. D., Kojima, M., … Iguchi, T. (2013). The Global Precipitation Measurement Mission. *Bulletin of the American Meteorological Society*, *95*(5), 701–722. https://doi.org/10.1175/BAMS-D-13-00164.1

Hou, A. Y., Skofronick-Jackson, G., Kummerow, C. D., & Shepherd, J. M. (2008). Global precipitation measurement. In S. Michaelides (Ed.), *Precipitation: Advances in Measurement, Estimation and Prediction* (pp. 131–169). Retrieved from http://link.springer.com/chapter/10.1007/978-3-540-77655-0_6

Houghton, H. G. (1951). On the Physics of Clouds and Precipitation. In *Compendium of Meteorology* (pp. 165–181). https://doi.org/10.1007/978-1-940033-70-9_14

Iguchi, T., Seto, S., Meneghini, R., Yoshida, N., Awaka, J., Le, M., … Kubota, T. (2016). GPM/DPR Level-2 Algorithm Theoretical Basis Document. Retrieved July 6, 2018, from http://www.eorc.jaxa.jp/GPM/doc/algorithm/ATBD_DPR_2015_whole_2a.pdf

IPCC. (2014). Summary for Policymakers. Retrieved September 27, 2016, from http://www.ipcc.ch/pdf/assessment-report/ar5/wg2/ar5_wgII_spm_en.pdf

Kirstetter, P.-E., Andrieu, H., Boudevillain, B., & Delrieu, G. (2013). A Physically Based Identification of Vertical Profiles of Reflectivity from Volume Scan Radar Data. *Journal of Applied Meteorology and Climatology*, *52*(7), 1645–1663. https://doi.org/10.1175/JAMC-D-12-0228.1

Kirstetter, P.-E., Gourley, J. J., Hong, Y., Zhang, J., Moazamigoodarzi, S., Langston, C., & Arthur, A. (2015a). Probabilistic precipitation rate estimates with ground-based radar networks. *Water Resources Research*, *51*(3), 1422–1442. https://doi.org/10.1002/2014WR015672

Kirstetter, P.-E., Hong, Y., Gourley, J. J., Schwaller, M., Petersen, W., & Cao, Q. (2015b). Impact of sub-pixel rainfall variability on spaceborne precipitation estimation: evaluating the TRMM 2A25 product. *Quarterly Journal of the Royal Meteorological Society*, *141*(688), 953–966. https://doi.org/10.1002/qj.2416

Kobayashi, K., Shige, S., & Yamamoto, M. K. (2018). Vertical gradient of stratiform radar reflectivity below the bright band from the tropics to the extratropical latitudes seen by GPM. *Quarterly Journal of the Royal Meteorological Society*, *0*(ja). https://doi.org/10.1002/qj.3271

Kumjian, M. R., & Prat, O. P. (2014). The Impact of Raindrop Collisional Processes on the Polarimetric Radar Variables. *Journal of the Atmospheric Sciences*, *71*(8), 3052–3067. https://doi.org/10.1175/JAS-D-13-0357.1

Kumjian, M. R., Ryzhkov, A. V., Trömel, S., Diederich, K., Mühlbauer, K., & Simmer, C. (2012). Abstract: Retrievals of Warm-Rain Microphysics Using X-Band Polarimetric Radar Data (92nd American Meteorological Society Annual Meeting (January 22-26, 2012)). Retrieved July 7, 2018, from https://ams.confex.com/ams/92Annual/webprogram/Paper206846.html

Le, M., & Chandrasekar, V. (2013). Hydrometeor Profile Characterization Method for Dual-Frequency Precipitation Radar Onboard the GPM. *IEEE Transactions on Geoscience and Remote Sensing*, *51*(6), 3648–3658. https://doi.org/10.1109/TGRS.2012.2224352

Lebel, T., Cappelaere, B., Galle, S., Hanan, N., Kergoat, L., Levis, S., … Seguis, L. (2009). AMMA-CATCH studies in the Sahelian region of West-Africa: An overview. *Journal of Hydrology*, *375*(1), 3–13. https://doi.org/10.1016/j.jhydrol.2009.03.020

Liu, C., & Zipser, E. J. (2009). "Warm Rain" in the Tropics: Seasonal and Regional Distributions Based on 9 yr of TRMM Data. *Journal of Climate*, *22*(3), 767–779. https://doi.org/10.1175/2008JCLI2641.1

Maggioni, V., Sapiano, M. R. P., & Adler, R. F. (2016). Estimating Uncertainties in High-Resolution Satellite Precipitation Products: Systematic or Random Error? *Journal of Hydrometeorology*, *17*(4), 1119–1129. https://doi.org/10.1175/JHM-D-15-0094.1

Meneghini, R., Meneghini, R., & Kozu, T. (1990). *Spaceborne Weather Radar*. Boston: Artech House Publishers.

Morris, K. R., & Schwaller, M. (2011). *Sensitivity of Spaceborne and Ground Radar Comparison Results to Data Analysis Methods and Constraints*. Retrieved from https://core.ac.uk/display/10560225

National Academies of Sciences, E. (2018). *Thriving on Our Changing Planet: A Decadal Strategy for Earth Observation from Space*. https://doi.org/10.17226/24938

Petersen, W. A., Carey, L. D., Rutledge, S. A., Knievel, J. C., Johnson, R. H., Doesken, N. J., … Weaver, J. F. (1999). Mesoscale and Radar Observations of the Fort Collins Flash Flood of 28 July 1997. *Bulletin of the American Meteorological Society*, *80*(2), 191–216. https://doi.org/10.1175/1520-0477(1999)080<0191:MAROOT>2.0.CO;2

Porcacchia, L., Kirstetter, P. E., Gourley, J. J., Maggioni, V., Cheong, B. L., & Anagnostou, M. N. (2017). Toward a Polarimetric Radar Classification Scheme for Coalescence-Dominant Precipitation: Application to Complex Terrain. *Journal of Hydrometeorology*, *18*(12), 3199–3215. https://doi.org/10.1175/JHM-D-17-0016.1

Saharia, M., Kirstetter, P.-E., Vergara, H., Gourley, J. J., & Hong, Y. (2017). Characterization of floods in the United States. *Journal of Hydrology*, *548*, 524–535. https://doi.org/10.1016/j.jhydrol.2017.03.010

Stephens, G. L., & Kummerow, C. D. (2007). The Remote Sensing of Clouds and Precipitation from Space: A Review. *Journal of the Atmospheric Sciences*, *64*(11), 3742–3765. https://doi.org/10.1175/2006JAS2375.1

Stoelinga, M. T., Stewart, R. E., Thompson, G., & Thériault, J. M. (2013). Microphysical Processes Within Winter Orographic Cloud and Precipitation Systems. In *Springer Atmospheric Sciences*. *Mountain Weather Research and Forecasting* (pp. 345–408). https://doi.org/10.1007/978-94-007-4098-3_7

Terti, G., Ruin, I., Gourley, J. J., Kirstetter, P., Flamig, Z., Blanchet, J., … Anquetin, S. (2017). Toward Probabilistic Prediction of Flash Flood Human Impacts. *Risk Analysis*, *0*(0). https://doi.org/10.1111/risa.12921

Vitale, J., & Ryan, T. (2013). Operational Recognition of High Precipitation Efficiency and Low - Echo - Centroid Convection. Retrieved September 14, 2016, from http://www.nwas.org/jom/articles/2013/2013-JOM12/2013-JOM12.pdf

Warner, T. T., Brandes, E. A., Sun, J., Yates, D. N., & Mueller, C. K. (2000). Prediction of a Flash Flood in Complex Terrain. Part I: A Comparison of Rainfall Estimates from Radar, and Very Short Range Rainfall Simulations from a Dynamic Model and an Automated Algorithmic System. *Journal of Applied Meteorology*, *39*(6), 797–814. https://doi.org/10.1175/1520-0450(2000)039<0797:POAFFI>2.0.CO;2

Wolfensberger, D., Scipion, D., & Berne, A. (2016). Detection and characterization of the melting layer based on polarimetric radar scans. *Quarterly Journal of the Royal Meteorological Society*, *142*, 108–124. https://doi.org/10.1002/qj.2672

Xu, X., Howard, K., & Zhang, J. (2008). An Automated Radar Technique for the Identification of Tropical Precipitation. *Journal of Hydrometeorology*, *9*(5), 885–902. https://doi.org/10.1175/2007JHM954.1

Zawadzki, I., Szyrmer, W., Bell, C., & Fabry, F. (2005). Modeling of the Melting Layer. Part III: The Density Effect. *Journal of the Atmospheric Sciences*, *62*(10), 3705–3723. https://doi.org/10.1175/JAS3563.1

Zhang, J., Howard, K., Langston, C., Kaney, B., Qi, Y., Tang, L., … Kitzmiller, D. (2015). Multi-Radar Multi-Sensor (MRMS) Quantitative Precipitation Estimation: Initial Operating Capabilities. *Bulletin of the American Meteorological Society*, *97*(4), 621–638. https://doi.org/10.1175/BAMS-D-14-00174.1

Zhang, J., Qi, Y., Kingsmill, D., & Howard, K. (2012). Radar-Based Quantitative Precipitation Estimation for the Cool Season in Complex Terrain: Case Studies from the NOAA Hydrometeorology

Testbed. *Journal of Hydrometeorology*, *13*(6), 1836–1854. https://doi.org/10.1175/JHM-D-11-0145.1

Zhang, J., Qi, Y., Langston, C., Kaney, B., & Howard, K. (2014). A Real-Time Algorithm for Merging Radar QPEs with Rain Gauge Observations and Orographic Precipitation Climatology. *Journal of Hydrometeorology*, *15*(5), 1794–1809. https://doi.org/10.1175/JHM-D-13-0163.1

Table Captions

Table 1. Reflectivity and DFR slopes in the liquid layer and the ice layer for CC-dominant and NCC profiles.

Table 2. Macrophysical properties for CC-dominant and NCC profiles.

Figure Captions

Figure 1. Distribution of WSR-88D GRs (circles) and the 06/02/2015 GPM orbit track (strip) over the CONUS (a); schematics of a DPR beam intercepting GR beams at two antenna elevations (b); schematics of a waffle of GR bins for a fixed antenna elevation (c).

Figure 2. (ΔZ_h, ΔZ_{dr}) parameter space relating ΔZ_h and ΔZ_{dr} in the liquid layer.

Figure 3. Precipitation event of 09/03/2014 at latitude 45.32 N and longitude 98.36 W. Vertical profiles of Z_h (a), Z_{dr} (b), $D_{m,GR}$ (c) from GR. Vertical profiles of Z_m(Ku), Z_e(Ku) (d), Z_m(Ka), Z_e(Ka) (e), DFR_m, DFR_e (f) and $D_{m,DPR}$ (g) from DPR.

Figure 4. Precipitation event of 09/03/2014 latitude 45.32 N and longitude 98.36 W. Maps of DPR reflectivity cross track at Ka-band (a) and Ku-band (b). Maps of DPR reflectivity along track at Ka-band (c) and Ku-band (d).

Figure 5. Spatial and seasonal distribution of CC-dominant and NCC profiles.

Figure 6. Conditional distributions of vertical profiles of Z_m(Ku) (a), Z_m(Ka) (b), and DFR_m (c) for CC-dominant and NCC profiles.

Figure 7. Distributions of reflectivity and DFR_m slopes for CC-dominant and NCC profiles. Liquid layer: Z_m(Ku) slope (a), Z_m(Ka) slope (b), and DFR_m slope (c). Ice layer: Z_m(Ku) slope (d), Z_m(Ka) slope (e), and DFR_m slope (f).

Figure 8. Distributions of cloud macrophyscial properties for CC-dominant and NCC profiles:

storm top height (STH) (a), ice layer depth (b), melting layer (ML) depth (c), liquid layer depth (d), Ku-band enhancement (e), and Ka-band enhancement (f).

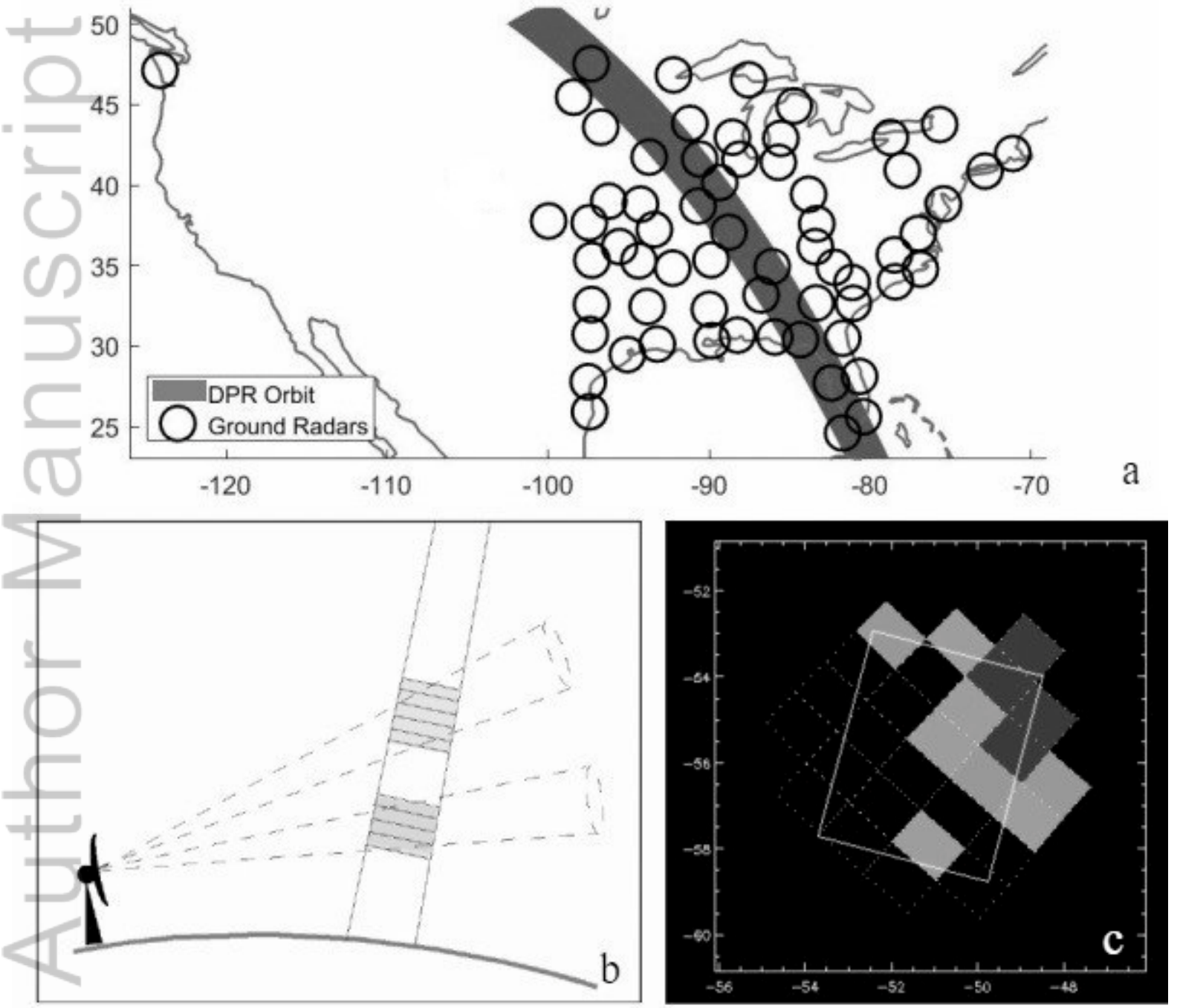

QJ_3611_Figure1.png

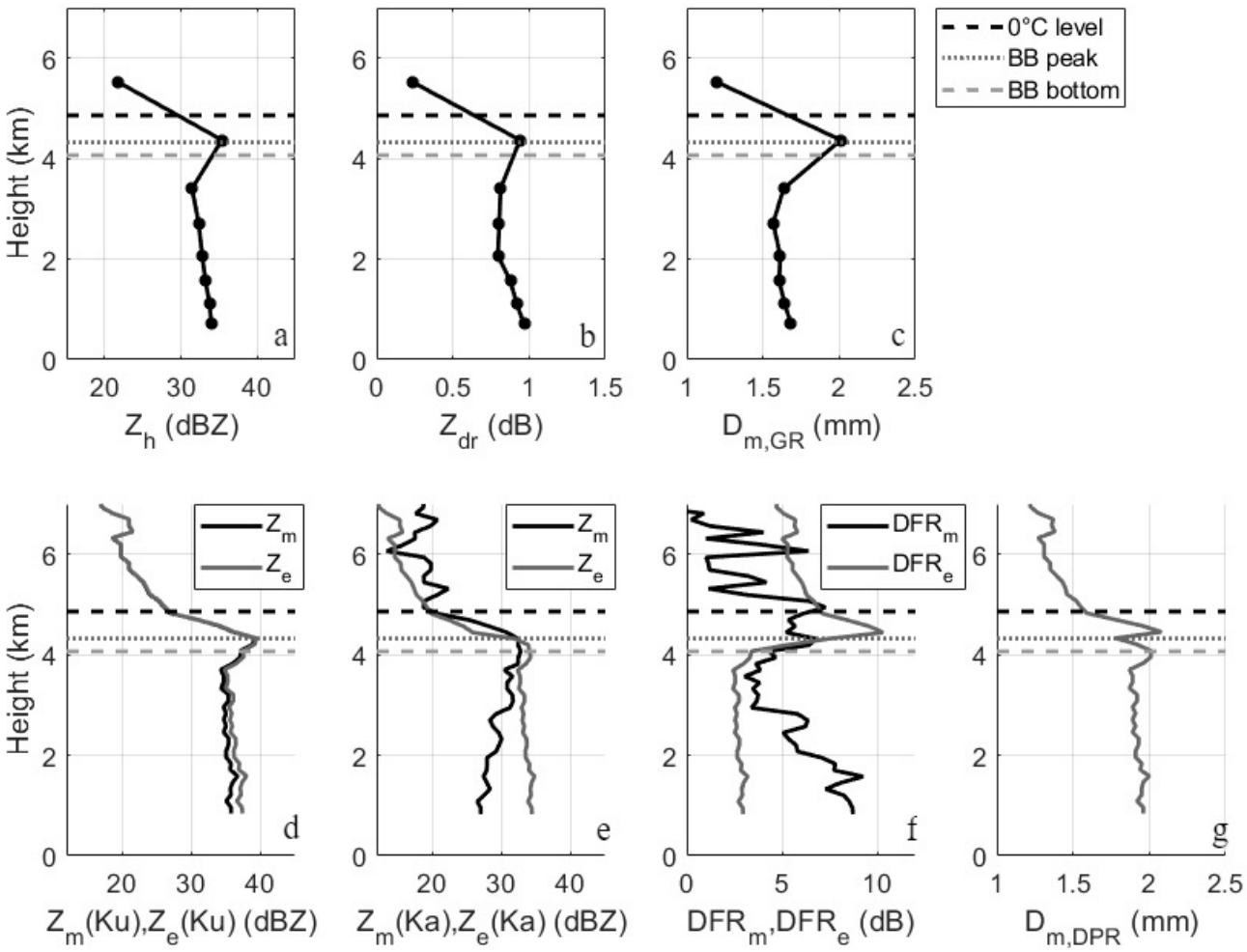

QJ_3611_Figure3.png

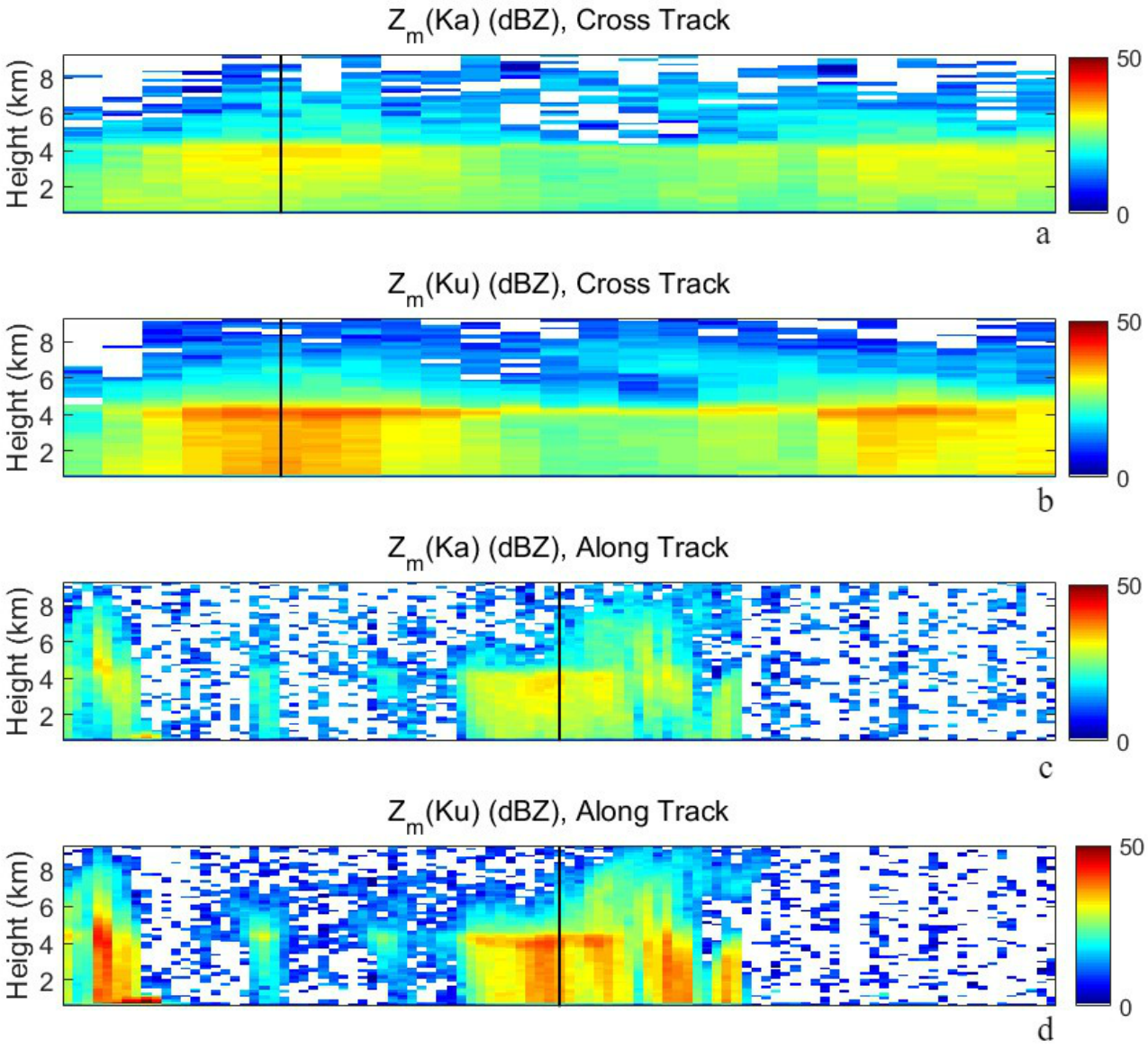

QJ_3611_Figure4.png

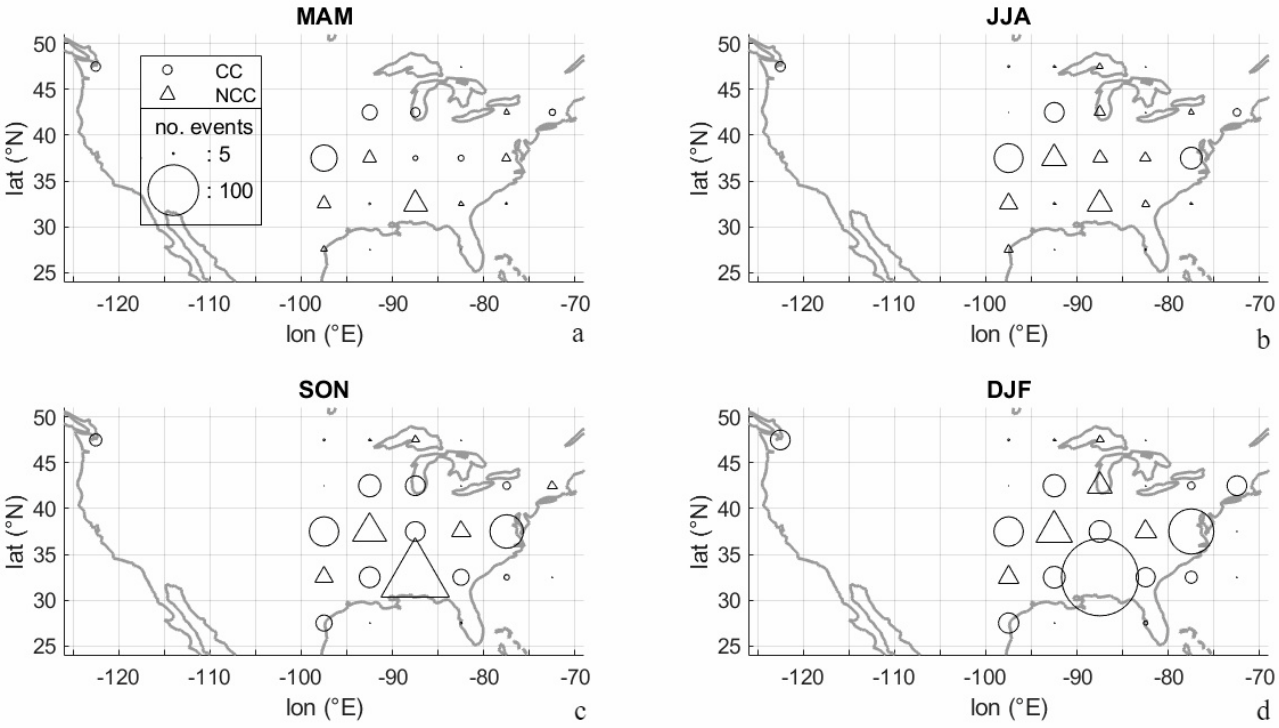

QJ_3611_Figure5.png

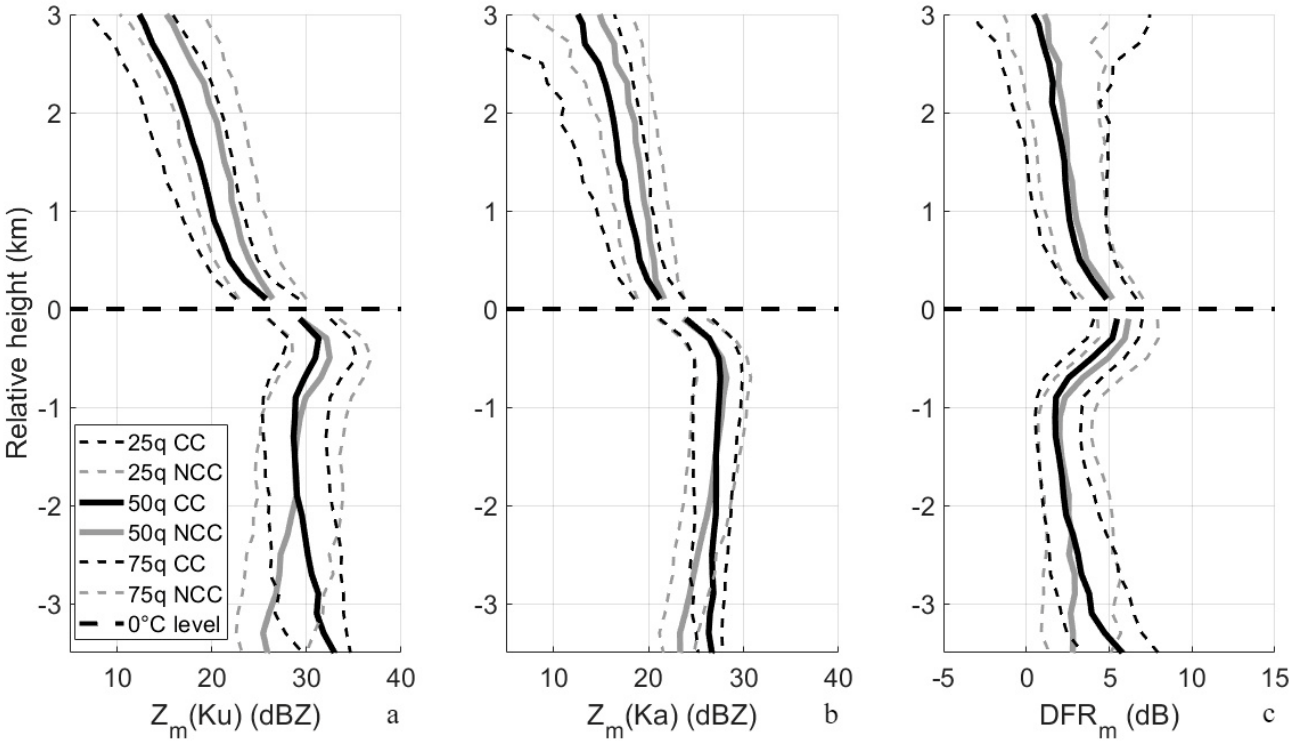

QJ_3611_Figure6.png

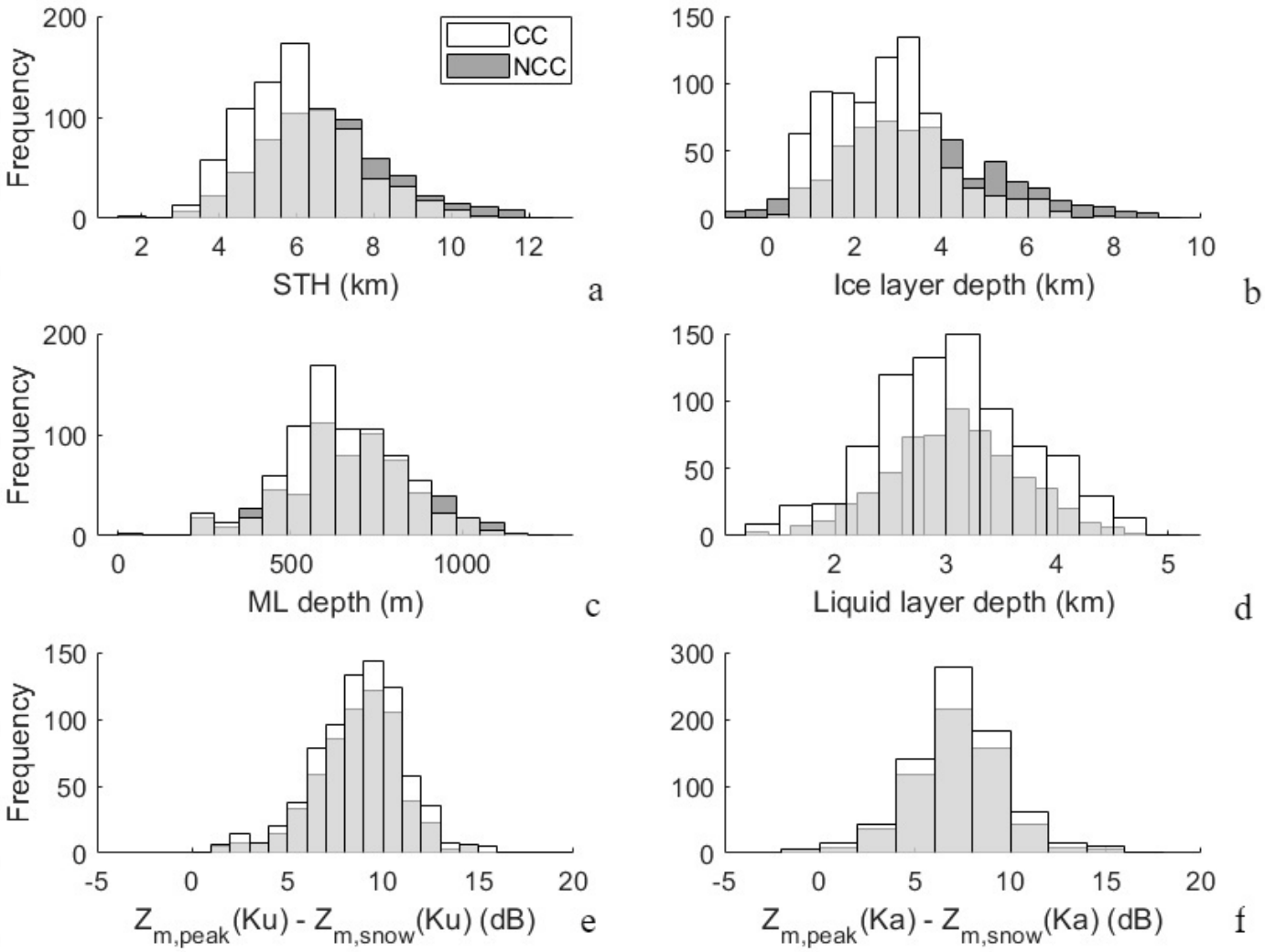

QJ_3611_Figure8.png

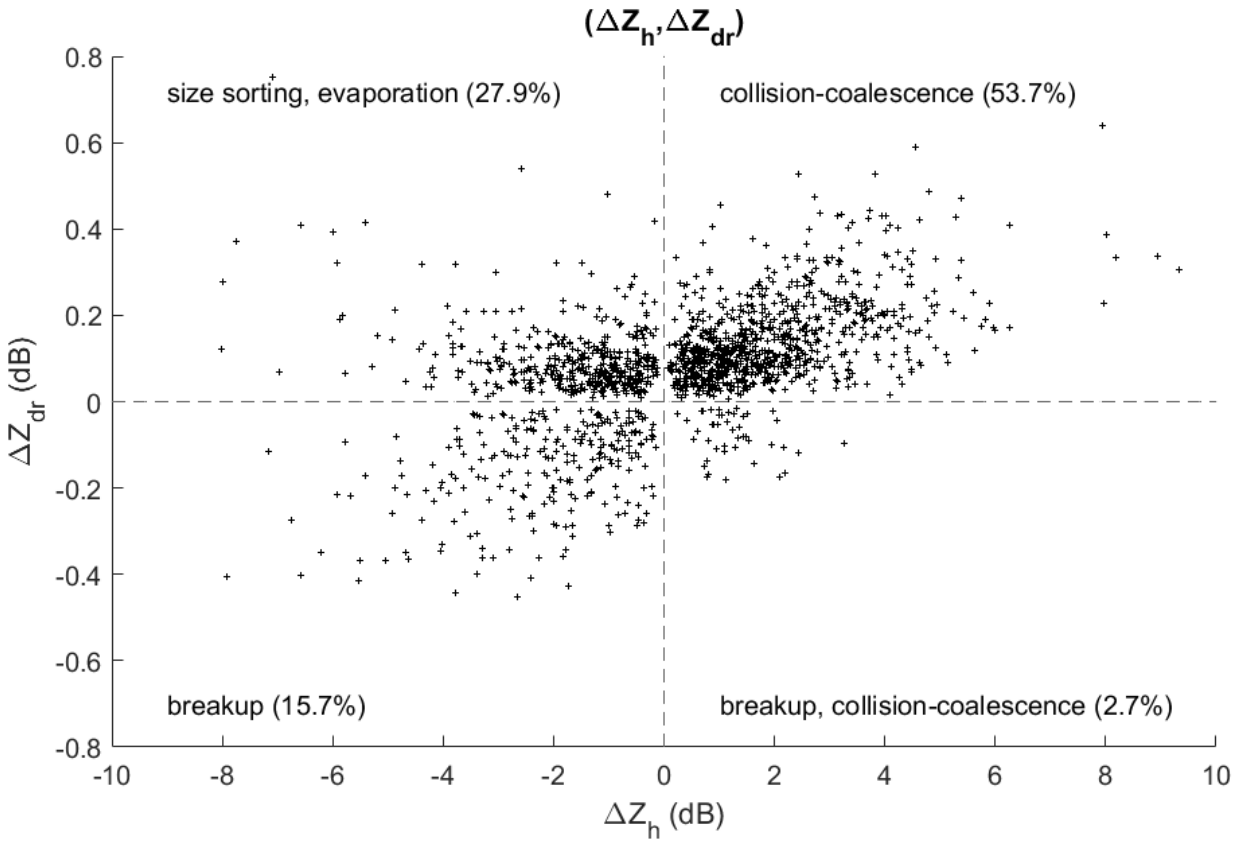

Figure 2. (ΔZ_h, ΔZ_{dr}) parameter space relating ΔZ_h and ΔZ_{dr} in the liquid layer.

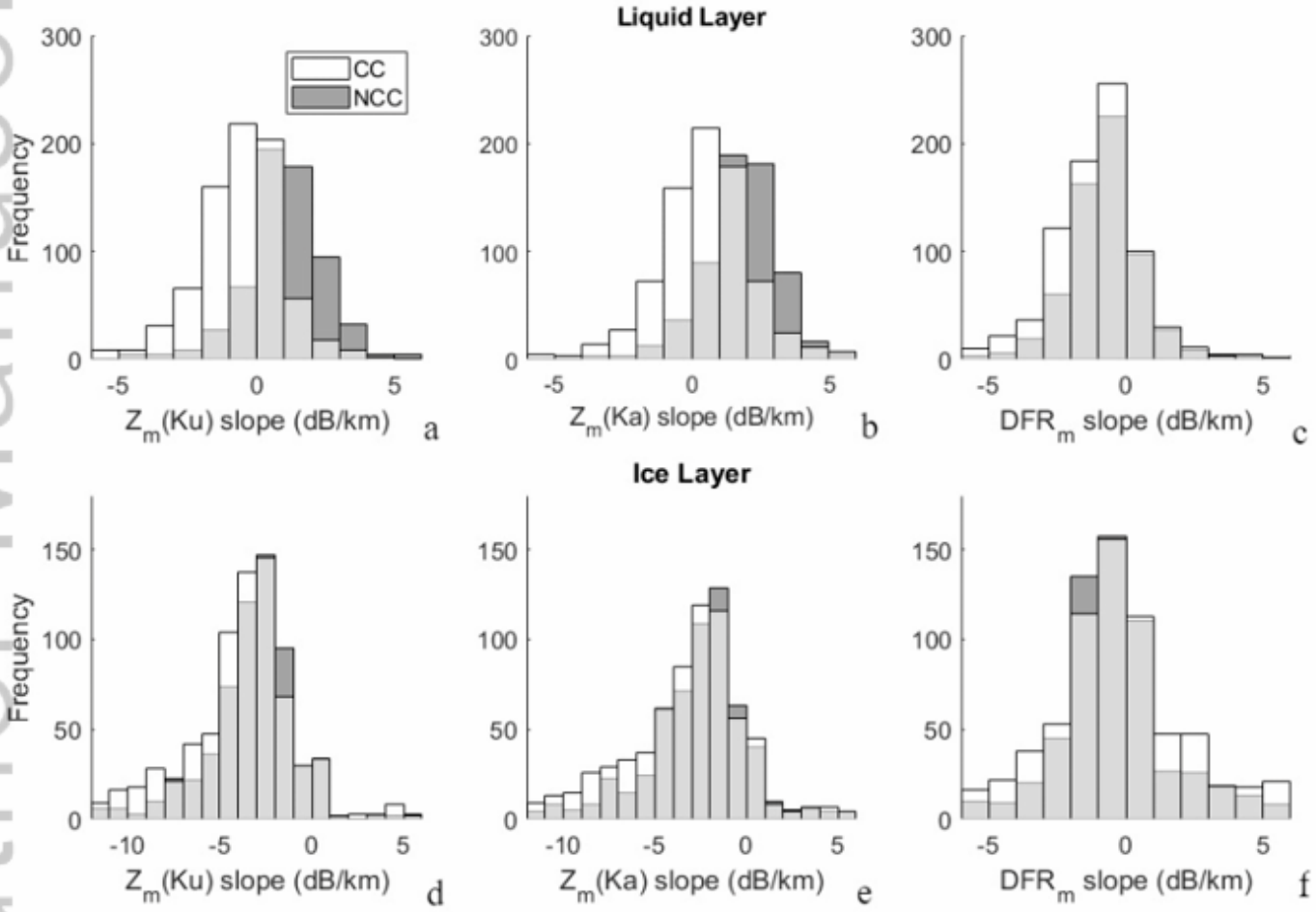

QJ_3611_Figure 7.PNG

Graphical Abstract

Title: Investigating the GPM Dual-Frequency Precipitation Radar Signatures of Low-Level Precipitation Enhancement

Authors**:** Leonardo Porcacchia*, Pierre-Emmanuel Kirstetter, Viviana Maggioni, Simone Tanelli

Key Findings:

- Low-level precipitation enhancement due to dominance of collision-coalescence in the cloud liquid layer is observed in mixed-phased clouds at mid-latitudes in the central/eastern United States during June 2014 – May 2018;
- Collision-coalescence-dominant profiles show distinguishing features in the GPM DPR retrievals when compared to NCC profiles (stratiform precipitation), particularly, characteristic vertical slopes of reflectivity at Ku- and Ka-band in the liquid layer;
- The GPM DPR level 2 retrieval algorithm is not adequate to parametrize the DSD of precipitation columns dominated by collision-coalescence.

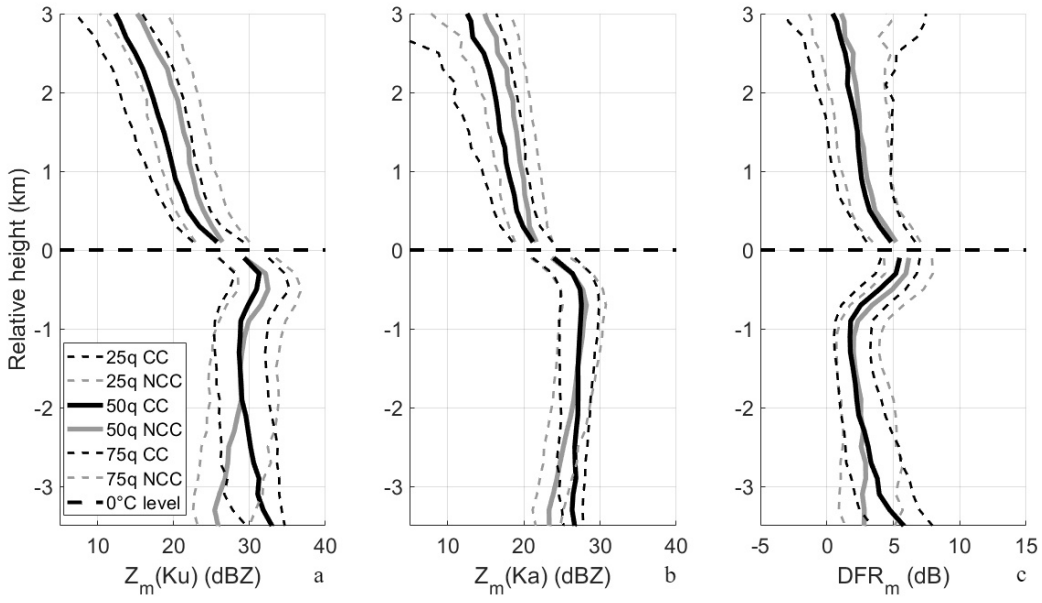

Figure. Conditional distributions of vertical profiles of Z_m(Ku), Z_m(Ka), and DFR_m for CC-dominant and NCC profiles.

Table 1. Reflectivity and DFR_m slopes in the liquid layer and the ice layer for CC-dominant and NCC profiles.

			median	SD	2KS p-value
Liquid layer	Z_m(Ku) slope (dB/km)	CC	-0.47	2.07	<1e-15
		NCC	1.03	3.38	
	Z_m(Ka) slope (dB/km)	CC	0.52	2.52	<1e-15
		NCC	1.89	4.73	
	DFR_m slope (dB/km)	CC	-0.96	2.83	2.4e-05
		NCC	-0.76	4.21	
Ice layer	Z_m(Ku) slope (dB/km)	CC	-3.60	5.49	9.3e-07
		NCC	-3.01	4.76	
	Z_m(Ka) slope (dB/km)	CC	-3.13	8.19	2.2e-06
		NCC	-2.32	5.89	
	DFR_m slope (dB/km)	CC	-0.40	6.77	7.4e-04
		NCC	-0.60	5.55	

Table 2. Macrophysical properties for CC-dominant and NCC profiles.

		median	SD	2KS p-value
STH (km)	CC	5.89	1.48	1.8e-15
	NCC	6.63	1.71	
Ice layer depth (km)	CC	2.69	1.36	3.3e-16
	NCC	3.33	1.86	
ML depth (m)	CC	638	168	3.6e-04
	NCC	689	187	
Liquid layer depth (km)	CC	3.05	0.68	4.8e-02
	NCC	3.08	0.59	
Ku enhancement (dB)	CC	7.54	4.06	9.7e-03
	NCC	8.35	3.93	
Ka enhancement (dB)	CC	6.18	3.58	0.14
	NCC	6.61	3.19	